

The *Chandra*/HETG view of NGC 1365 in a Compton-thick state

E. Nardini,^{1*} J. Gofford,^{1,2} J. N. Reeves,^{1,2} V. Braito,³ G. Risaliti,⁴ M. Costa¹

¹*Astrophysics Group, School of Physical and Geographical Sciences, Keele University, Keele, Staffordshire ST5 5BG, UK*

²*Department of Physics, University of Maryland Baltimore County, 1000 Hilltop Circle, Baltimore, MD 21250, USA*

³*INAF – Osservatorio Astronomico di Brera, via E. Bianchi 46, I-23807 Merate, Italy*

⁴*INAF – Osservatorio Astrofisico di Arcetri, L.go E. Fermi 5, I-50125 Firenze, Italy*

12 June 2021

ABSTRACT

We present the analysis of a *Chandra* High-Energy Transmission Grating (HETG) observation of the local Seyfert galaxy NGC 1365. The source, well known for its dramatic X-ray spectral variability, was caught in a reflection-dominated, Compton-thick state. The high spatial resolution afforded by *Chandra* allowed us to isolate the soft X-ray emission from the active nucleus, neglecting most of the contribution from the kpc-scale starburst ring. The HETG spectra thus revealed a wealth of He- and H-like lines from photoionized gas, whereas in larger aperture observations these are almost exclusively produced through collisional ionization in the circumnuclear environment. Once the residual thermal component is accounted for, the emission-line properties of the photoionized region close to the hard X-ray continuum source indicate that NGC 1365 has some similarities to the local population of obscured active galaxies. In spite of the limited overall data quality, several soft X-ray lines seem to have fairly broad profiles ($\sim 800\text{--}1300\text{ km s}^{-1}$ full-width at half maximum), and a range of outflow velocities (up to $\sim 1600\text{ km s}^{-1}$, but possibly reaching a few thousands km s^{-1}) appears to be involved. At higher energies, the $K\alpha$ fluorescence line from neutral iron is resolved with > 99 per cent confidence, and its width of $\sim 3000\text{ km s}^{-1}$ points to an origin from the same broad-line region clouds responsible for eclipsing the X-ray source and likely shielding the narrow-line region.

Key words: galaxies: active – X-rays: galaxies – galaxies: individual: NGC 1365 – line: identification

1 INTRODUCTION

Irrespective of their different optical properties and classification, the energy source of active galactic nuclei (AGN) is strongly suggested to be intrinsically the same (e.g. Antonucci & Miller 1985). When broad lines are lacking, a direct view of central engine would be prevented by a dusty absorber, covering a substantial, yet not complete fraction of the solid angle, and thus commonly envisaged as a toroidal structure (Krolik & Begelman 1988). The orientation-based idea that underlies AGN unification models (Antonucci 1993, and references therein) is still broadly accepted. While it was argued early on that the torus might well consist of individual *clouds*, the multiple pieces of observational evidence accumulated in the last decade imply that the circumnuclear environment in AGN is characterized by a large degree of clumpiness and inhomogeneity on various physical

scales, from tens of pc down to a few hundreds of gravitational radii ($r_g = GM_{\text{BH}}/c^2$) from the supermassive black hole (see Bianchi, Maiolino & Risaliti 2012; Netzer 2015 for recent overviews).

The nearby Seyfert galaxy NGC 1365 ($z \simeq 0.0055$) is an ideal object to probe the complexity of nuclear obscuration in AGN. Optically classified as a type 1.8 (Maiolino & Rieke 1995), NGC 1365 has been extensively studied in the X-rays for its exceptional variability, which makes it the most striking example of a changing-look AGN (Matt, Guainazzi & Maiolino 2003). Apparently due to a favourable line of sight, the inner accretion disc/X-ray corona system is seen through an erratic absorbing medium, whose marked column density gradients are betrayed by the random alternation of Compton-thin ($N_{\text{H}} < 10^{23}\text{ cm}^{-2}$) and Compton-thick ($N_{\text{H}} > 10^{24}\text{ cm}^{-2}$) states. The switch from transmission- to reflection-dominated spectra (and back) can take less than two days, involving the transit of a single cloud (Risaliti et al. 2007). This kind of eclipses not only sets a tight empir-

* E-mail: e.nardini@keele.ac.uk

ical limit to the size of the X-ray source (no larger than a few tens of r_g), but also provides an implicit measure of the distance and density of the intervening blobs (both indicative of the gas in the Broad Line Region; BLR), and reveals unique details about their shape (e.g. Maiolino et al. 2010). Besides this, in the Compton-thin regime NGC 1365 regularly exhibits four strong absorption lines in the ~ 6.7 – 8.3 keV band. Their spacing prompts an identification with the $K\alpha$ and $K\beta$ pairs from Fe XXV–XXVI, blueshifted by reason of an outflow velocity of $v_{\text{out}} \sim 1000$ – 5000 km s $^{-1}$, variable over timescales of weeks/months (Risaliti et al. 2005; Nardini et al., in preparation). These lines could just trace the high-ionization phase of a much more pervasive wind, possibly including all the manifest absorption components (Connolly, McHardy & Dwelly 2014; Braito et al. 2014).

Adding to the overall merit of NGC 1365 is one of the largest infrared luminosities ($L_{\text{IR}} \sim 10^{11} L_{\odot}$) among nearby, non-interacting galaxies. This mostly arises from the great number of star-forming clusters in the central ~ 2 – 3 kpc, disposed in an elongated ring around the nucleus (Alonso-Herrero et al. 2012, and references therein). The powerful starburst is also the main source of the observed soft X-ray emission ($E < 3$ keV), which is found to be constant in flux and shape. Indeed, the ~ 500 -ks high-resolution spectrum obtained by combining all the 2004 and 2007 data from the *XMM-Newton* Reflection Grating Spectrometer (RGS) is rife with collisionally ionized lines from the hot diffuse gas, at odds with a typical obscured Seyfert (Guainazzi et al. 2009). In this paper we report on two *Chandra* observations of NGC 1365 taken with the High-Energy Transmission Grating (HETG; Canizares et al. 2005) over a span of four days, during which the AGN remained in a heavily absorbed, Compton-thick state.

2 OBSERVATIONS AND DATA REDUCTION

NGC 1365 was observed twice by *Chandra* in 2012, on April 9 and three days later (ObsIDs 13920/1), for a total exposure of ~ 200 ks. After a series of six 15-ks snapshots in 2006 (Risaliti et al. 2007) and a previous one of the same length in 2002, these were the first observations of NGC 1365 at high spectral resolution with *Chandra*. The HETG consists of two sets of gratings, optimized for medium (MEG; 0.5–7 keV) and high (HEG; 0.8–10 keV) energies, respectively, and was used in combination with the Advanced CCD Imaging Spectrometer (ACIS-S) array. The data were reprocessed with the CIAO version 4.4 software package and the v4.4.9 Calibration Database (CALDB). For each observation, the MEG and HEG spectra were extracted from first-order events in both (± 1) diffraction arms. Redistribution matrices were created with the CIAO tool `mkgrmf`, while effective area files were obtained through the `fullgarf` script. The spectra and detector responses from the ± 1 orders were combined with the appropriate weights. Since the background is negligible, no correction was performed, and no systematic uncertainty was introduced.

After verifying that the two observations are consistent with each other, in order to improve the data quality for the subsequent analysis we also merged the spectra (and auxiliary files) from ObsIDs 13920/1 into a single one. It is worth noting that we adopted a narrower extraction strip than the

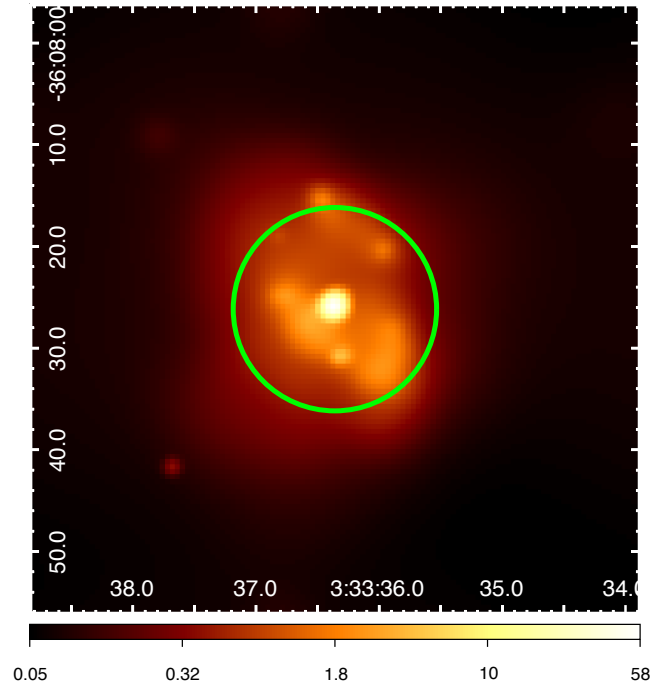


Figure 1. X-ray image of the central $1' \times 1'$ region of NGC 1365 in the 0.3–3 keV energy range (from ObsIDs 13920/1), showing the extent of the diffuse starburst emission and the aperture adopted (green circle, $10''$ radius). An adaptive smoothing has been applied following the same criteria of Wang et al. (2009).

default one ($20''$ instead of $35''$): this allowed us to exclude part of the diffuse X-ray emission associated with the star-forming ring of $\sim 15''$ diameter on kpc scale ($1'' \sim 90$ pc, Fig. 1; see also Wang et al. 2009), and at the same time to extend the final HEG spectrum up to ~ 8 keV. In all the spectral fits (carried out with XSPEC v12.8, with solar abundances from Wilms, Allen & McCray 2000) we considered the 0.5–5 keV (MEG) and 1.5–8 keV (HEG) energy ranges, over which a total of ~ 1580 and 1050 counts were collected, respectively. We initially binned the data to 2048 channels, corresponding to a $\Delta\lambda$ of 20 (MEG) and 10 mÅ (HEG), that is roughly the full width at half-maximum (FWHM) resolution. However, due to the limited number of counts, we further imposed a minimum of four counts per energy bin, and made use of the *C*-statistic (Cash 1979). Unless otherwise stated, the lines' energies are given in the rest frame of NGC 1365, and all the uncertainties correspond to the 90% confidence level for the single parameter of interest ($\Delta C = 2.71$). For simplicity, throughout this work we assumed a standard concordance cosmology with $H_0 = 70$ km s $^{-1}$ Mpc $^{-1}$, $\Omega_m = 0.27$, and $\Omega_\Lambda = 0.73$, although the luminosity distance entailed for NGC 1365 (~ 21 Mpc) slightly differs from the one based on Cepheid variables of $D = 18.6 \pm 1.9$ Mpc (Madore et al. 1998).

3 SPECTRAL ANALYSIS

The HETG spectra of NGC 1365 are shown in Fig. 2, compared to the brightest flux state ever reached by the source during an *XMM-Newton* observation performed only

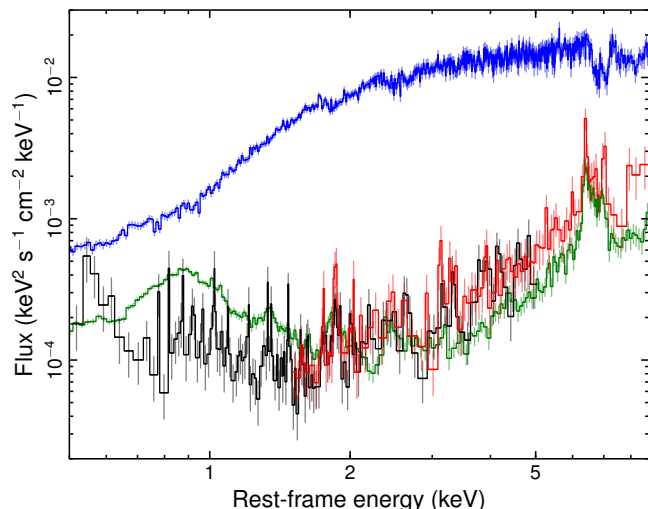


Figure 2. *Chandra* HETG spectra of NGC 1365, plotted in black (MEG) and red (HEG), respectively. The historical extremes of transmission- and reflection-dominated states are also shown for comparison. The source has the typical Compton-thick spectral shape at 2–10 keV, and is ~ 15 times dimmer than during the final part of the January 2013 *XMM-Newton* observation (blue), when the neutral column density dropped to $N_{\text{H}} \sim 10^{22} \text{ cm}^{-2}$. Indeed, the flux lies above the minimum reached in the 2007 *XMM-Newton* monitoring (green) just by a factor of ~ 1.8 . Note, however, that the narrower extraction region adopted for *Chandra* allowed us to disentangle the nuclear soft X-ray component from most of the circumnuclear starburst emission. (All the data were rebinned for display purposes).

nine months later in January 2013, when the column density towards the AGN was just about $N_{\text{H}} \sim 10^{22} \text{ cm}^{-2}$ (Braitto et al. 2014; Rivers et al. 2015). *Chandra* clearly met a Compton-thick state, exhibiting a faint and very hard ($\Gamma = -1.5$) continuum above 3 keV, which closely resembles the lowest reflection-dominated spectrum of the first *XMM-Newton* orbit in the 2007 five-day monitoring (Fig. 2; Risaliti et al. 2009a). In the following analysis, we first focus on the overall shape of the continuum, and then take into account the rich emission-line spectrum in the soft X-rays.

3.1 Baseline continuum

As a starting point we adopted a model that simply consists of three different AGN-related components: the primary power-law continuum, attenuated by a foreground screen of cold gas at rest in the source frame ($z = 0.005457$); reflection off the irradiated matter, described as a **pexrav** template (Magdziarz & Zdziarski 1995) with solar abundances, inclination of 45° , and variable strength; and a soft X-ray power law, which is required by the modest spectral rise below ~ 1.5 keV and is interpreted as the faint, scattered AGN continuum. The latter component can be fitted in several alternative ways, for instance as a thermal bremsstrahlung of $kT \sim 0.8$ keV, possibly associated with starburst-driven shocks. However, due to its negligible impact on the final results and to the small (~ 1 – 2 per cent) scattering efficiency implied, we retained for simplicity the link of this soft continuum with the AGN, thus assuming a common photon index for the various forms of reprocessed AGN emis-

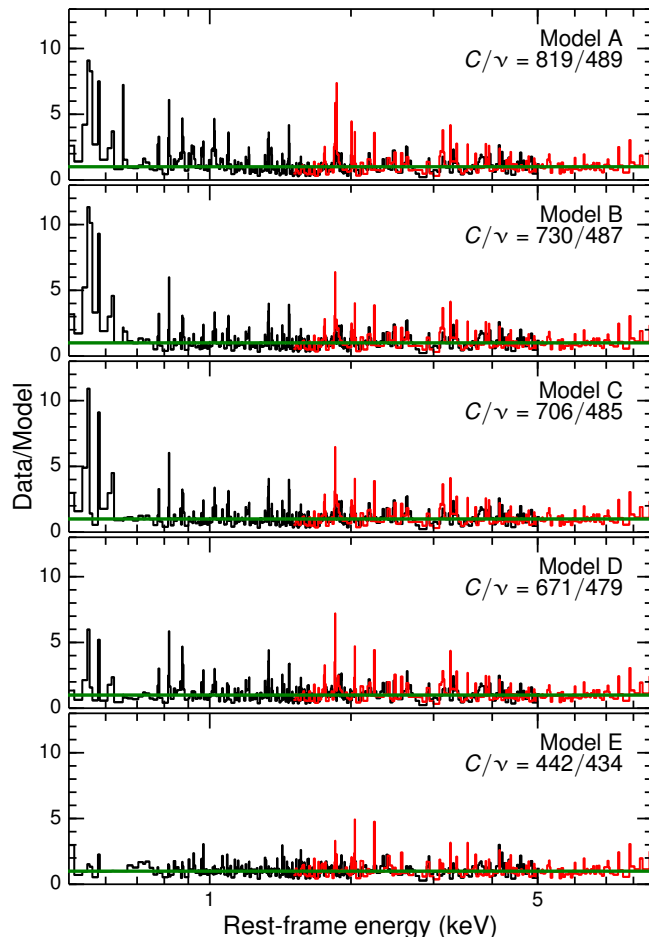


Figure 3. Fit residuals for the different models A–E (error bars are omitted for clarity). Once the AGN-related continuum components (i.e. transmitted, reflected and scattered) and the 6.4-keV iron K line are accounted for, a wealth of narrow emission features is left below ~ 4 keV (A). The addition of a thermal component from collisionally ionized gas returns an appreciable improvement around 1 keV (B), but any further thermal contribution is not strongly required (C,D). An adequate fit is obtained only after including individual Gaussian profiles to describe the 22 remaining emission lines detected with a statistical significance of at least 95 per cent (E).

sion (i.e. transmitted, reflected and scattered). This model (hereafter tagged as model A for brevity) and all the subsequent ones also include the Galactic column density (fixed to $N_{\text{H}} = 1.34 \times 10^{20} \text{ cm}^{-2}$; Kalberla et al. 2005) and the conspicuous iron fluorescence line around 6.4 keV, whose properties remain consistent throughout the fitting steps.

Model A already provides a good representation of the observed continuum, while the intrinsic power law is largely unconstrained at this stage, also because of the decreasing data quality at higher energies; the photon index and absorbing column were then frozen to the reasonable values of $\Gamma = 2$ and $N_{\text{H}} = 2 \times 10^{24} \text{ cm}^{-2}$. The overall statistics of $C/\nu = 819/489$ are still rather poor without accounting for the emission lines (Fig. 3). To check whether some of these can be ascribed to optically-thin, collisionally ionized plasma, which is indeed a major ingredient of the *XMM-Newton*/RGS spectrum (Guainazzi et al. 2009), we added

Table 1. Best-fit continuum parameters for the different models (A–E) and components: primary (1), scattered (2) and reflected (3) AGN emission, hot (4) and warm (5) thermal emission. N_{H} : foreground column density. Γ : power-law photon index. A : power-law normalization at 1 keV. R : reflection strength. kT : plasma temperature. Z : elemental abundance. EM: emission measure. (f) and (t) denote fixed and tied parameters. Each model also includes Galactic absorption and iron $K\alpha$ emission.

Component Parameter	Model A	Model B	Model C	Model D	Model E
(1) powerlaw₁					
N_{H} (10^{22} cm^{-2})	200(f)	200(f)	200(f)	200(f)	140^{+19}_{-12}
Γ	2.0(f)	2.0(f)	2.0(f)	2.0(f)	$2.10^{+0.05}_{-0.06}$
A ($10^{-4} \text{ cm}^{-2} \text{ s}^{-1} \text{ keV}^{-1}$)	77^{+22}_{-20}	60^{+21}_{-19}	58^{+21}_{-18}	46^{+20}_{-18}	44^{+3}_{-2}
(2) powerlaw₂					
Γ	2.0(t)	2.0(t)	2.0(t)	—	2.10(t)
A ($10^{-4} \text{ cm}^{-2} \text{ s}^{-1} \text{ keV}^{-1}$)	1.01 ± 0.06	0.71 ± 0.08	$0.68^{+0.09}_{-0.08}$	—	$0.54^{+0.06}_{-0.05}$
(3) pexrav					
Γ	2.0(t)	2.0(t)	2.0(t)	2.0(t)	2.10(t)
R	$0.50^{+0.20}_{-0.13}$	$0.74^{+0.38}_{-0.21}$	$0.78^{+0.41}_{-0.22}$	$1.24^{+0.88}_{-0.40}$	$1.01^{+0.16}_{-0.13}$
(4) apec₁					
N_{H} (10^{22} cm^{-2})	—	—	—	< 0.08	—
kT (keV)	—	$0.94^{+0.07}_{-0.09}$	$0.96^{+0.07}_{-0.08}$	$1.20^{+0.10}_{-0.11}$	$0.99^{+0.08}_{-0.09}$
Z_{O} (Z_{\odot})	—	1.0(f)	1.0(f)	$0.03^{+0.04}_{-0.02}$	1.0(f)
Z_{Ne} (Z_{\odot})	—	1.0(f)	1.0(f)	$0.17^{+0.33}_{-0.13}$	1.0(f)
Z_{Mg} (Z_{\odot})	—	1.0(f)	1.0(f)	$0.36^{+0.22}_{-0.17}$	1.0(f)
Z_{Si} (Z_{\odot})	—	1.0(f)	1.0(f)	$0.49^{+0.18}_{-0.15}$	1.0(f)
Z_{Fe} (Z_{\odot})	—	1.0(f)	1.0(f)	$0.05^{+0.03}_{-0.05}$	1.0(f)
EM (10^{63} cm^{-3})	—	0.25 ± 0.06	$0.25^{+0.06}_{-0.05}$	$1.86^{+0.23}_{-0.21}$	$0.18^{+0.05}_{-0.04}$
(5) apec₂					
N_{H} (10^{22} cm^{-2})	—	—	—	< 0.35	—
kT (keV)	—	—	$0.14^{+0.04}_{-0.03}$	$0.15^{+0.10}_{-0.05}$	—
EM (10^{63} cm^{-3})	—	—	$0.55^{+0.46}_{-0.32}$	$> 5.7^a$	—
Fit statistic C/ν	819/489	730/487	706/485	671/479	442/434

Notes: ^aDue to the fact that the peak temperature of this component falls outside the fitting range, the emission measure is largely degenerate with the column density, so that no sensible upper limit can be obtained.

an **apec** thermal component (Smith et al. 2001) with solar abundances. In this scenario, the ionization is driven by the impact of free electrons with a temperature comparable with the energy of the observed lines. The new fit (model B) brings a substantial improvement, with $\Delta C = -89$ for the loss of two degrees of freedom only, taken by the plasma temperature $kT \simeq 0.95$ keV and emission measure.¹ The most affected is the ~ 0.6 – 1.2 keV (10 – 20 Å) range, where there are hints of iron L-shell emission, mainly due to $3d \rightarrow 2p$ transitions from Fe XVIII–XXIII. This hot gas can be naturally identified with the residual contamination from the circumnuclear star formation (Fig. 1). The related continuum is much fainter than in the large-aperture RGS data (see also Fig. 2), and the contribution to the most prominent features is no larger than ~ 30 – 40 per cent in the case of Ly α lines from O VIII, Ne X, and Mg XII. We therefore introduced a second **apec** component of different temperature, but this is remarkably cold ($kT \simeq 0.15$ keV; Table 1) and simply imparts minor changes to the noisy lower end of the MEG spectrum ($C/\nu = 706/485$; model C). Apparent structures

compatible with the He-like triplets from Mg XI, Si XIII and Ar XVII are left unexplained, but no other zone of thermal emission is statistically required.

As an ultimate attempt to explore the significance of collisionally ionized plasma, we also allowed for variable abundances (tied between the two components) for all the key α -elements (O, Ne, Mg and Si) plus Fe, and for the possible column density enshrouding each star-forming region. The scattered AGN continuum was neglected to avoid any degeneracies (model D). The same set of assumptions was successfully applied by Guainazzi et al. (2009) in reproducing both the RGS and the previous *Chandra*/ACIS spectra of NGC 1365. With respect to their description, in the HETG data the separation between the plasma temperatures is much more pronounced, ~ 0.15 – 1.2 keV against ~ 0.3 – 0.7 keV, while absolute and relative abundances are rather similar (once the conversion between the adopted solar standards is applied). In any case, the global statistics only undergo a scarce decrease ($\Delta C = -35$ for $\Delta\nu = -6$), and the fit stays far from being satisfactory ($C/\nu = 671/479$). The full details are listed in Table 1. Equivalent results were achieved by letting vary a common α -element metallicity over the two regions ($Z_{\alpha} \sim 0.5$ and 0.03).

¹ The emission measure (in cm^{-3}) is defined as $\text{EM} = \int n_e n_{\text{H}} dV$, where n_e and n_{H} are the electron and hydrogen densities.

Table 2. Statistically significant emission lines in the *Chandra* HETG spectra, after accounting for the collisional component. The most plausible identifications are also listed. (f), (i), and (r) refer to forbidden, intercombination and resonance transitions for He-like species. (u) stands for unresolved ($\sigma = 2$ eV is then assumed). Note that the equivalent widths (EW) of broad features should not be taken at face value, since in most cases these are blends of two (or more) narrow lines (see the text for a thorough discussion).

	E_{obs} (eV)	σ (eV)	Flux ($10^{-6} \text{ s}^{-1} \text{ cm}^{-2}$)	EW (eV)	Transition	E_{lab} (eV)	$\Delta C/\Delta\nu$
1.	555^{+9}_{-8}	21^{+13}_{-7}	93^{+37}_{-32}	410^{+270}_{-220}	O v K α O VII He α (f)	554^a 561^b	54/3
2.	618^{+3}_{-2}	2(u)	11^{+11}_{-7}	39^{+39}_{-33}	O v K β	621^a	10/2
3.	655^{+2}_{-3}	2(u)	$7.0^{+7.5}_{-5.3}$	37 ± 34	O VIII Ly α	654^b	6/2
4.	778^{+3}_{-2}	2(u)	$2.9^{+2.8}_{-2.0}$	18 ± 15	O VIII Ly β Fe XVIII 3s \rightarrow 2p	775^b 775^c	9/2
5.	819^{+1}_{-2}	2(u)	$3.7^{+2.8}_{-2.1}$	22 ± 18	O VIII Ly γ Fe XIX 3s \rightarrow 2p	817^b 822^c	15/2
6.	874^{+6}_{-4}	6^{+9}_{-3}	$4.2^{+2.8}_{-2.3}$	26^{+23}_{-18}	O VIII RRC Fe XVIII 3d \rightarrow 2p	871^b 873^c	12/3
7.	1024 ± 4	6^{+7}_{-3}	$2.9^{+1.8}_{-1.5}$	24^{+22}_{-17}	Ne x Ly α	1022^b	14/3
8.	1096^{+2}_{-6}	2(u)	$0.9^{+1.0}_{-0.7}$	11^{+10}_{-8}	Ne IX He β (r)	1074^b	6/2
9.	1205 ± 6	8^{+7}_{-4}	$1.4^{+1.0}_{-0.8}$	24 ± 17	Ne x Ly β	1211^b	11/3
10.	1334^{+1}_{-2}	2(u)	$1.4^{+0.9}_{-0.6}$	26 ± 15	Mg XI He α (f)	1331^b	24/2
11.	1356 ± 3	2(u)	$0.6^{+0.6}_{-0.5}$	10^{+12}_{-9}	Mg XI He α (r)	1352^b	6/2
12.	1476 ± 1	2(u)	$1.2^{+0.5}_{-0.4}$	29^{+17}_{-14}	Mg XII Ly α	1473^b	42/2
13.	1756^{+7}_{-6}	2(u)	0.4 ± 2	10^{+10}_{-7}	Mg XII Ly β	1745^b	9/2
14.	1864^{+8}_{-7}	24^{+9}_{-6}	2.8 ± 0.7	96^{+67}_{-36}	Si XIII He α (r)	1865^b	62/3
15.	2006^{+2}_{-3}	2(u)	0.5 ± 0.3	19^{+18}_{-15}	Si XIV Ly α	2006^b	10/2
16.	2187^{+7}_{-6}	2(u)	$0.9^{+0.5}_{-0.6}$	40^{+49}_{-31}	Si XIII He β (r)	2183^b	9/2
17.	2475^{+8}_{-5}	2(u)	$0.9^{+0.7}_{-0.5}$	41^{+53}_{-34}	S XV He α (r)	2461^b	11/2
18.	2630 ± 20	27^{+26}_{-19}	$2.0^{+1.1}_{-1.0}$	100^{+150}_{-80}	S XVI Ly α	2623^b	15/3
19.	3138^{+13}_{-11}	19^{+14}_{-10}	$1.7^{+0.8}_{-0.7}$	83^{+110}_{-42}	Ar XVII He α (r)	3140^b	23/3
20.	3310^{+34}_{-31}	54^{+25}_{-14}	$2.0^{+1.1}_{-0.9}$	105^{+205}_{-75}	Ar XVIII Ly α	3323^b	15/2
21.	3873^{+28}_{-30}	83^{+67}_{-22}	$2.8^{+0.6}_{-0.9}$	160^{+540}_{-140}	Ca XIX He α (f) Ca XIX He α (i) Ca XIX He α (r)	3861^b 3883^b 3902^b	17/3
22.	6404^{+13}_{-14}	24^{+17}_{-12}	$7.0^{+2.8}_{-2.4}$	205^{+80}_{-70}	Fe I K α	6403^b	38/3

References: ^aKaastra et al. (2004); ^bNIST (<http://physics.nist.gov/asd>); ^cCHIANTI (Landi et al. 2012).

Incidentally, we note that model D actually delivers a fairly good fit ($C/\nu = 513/488$) of the zeroth-order spectrum at CCD resolution,² although with slightly adjusted values ($kT \sim 0.9$ and 0.3 keV, $N_{\text{H}} \sim 1.5$ and $< 0.2 \times 10^{22} \text{ cm}^{-2}$; abundances are poorly constrained but are consistent with being solar). We conclude that the copious line emission revealed by the *Chandra*/HETG observations is dominated by photoionized gas directly exposed to the radiation field of the AGN, which is clearly brought out for the first time.

3.2 Emission lines

While several star-forming regions are present within in the inner kpc, their weak soft X-ray emission precludes an accurate determination of the full range of properties (e.g. tem-

peratures and abundances) of the hot diffuse gas. We therefore built on model B, with a single thermal component of solar metallicity besides the transmitted, reflected and scattered AGN continua. A Gaussian profile was then added for any residual emission line, provided that each inclusion resulted in a $\Delta C = -6.0$ or -7.8 , corresponding to the 95 per cent confidence level for either two or three parameters of interest (model E). Following this criterion, which is less stringent than usual but is more appropriate to the signal to noise of the current data, 22 lines are detected (Table 2). At a first glance, based on the most likely identifications, all the main transitions of α -elements from O to Ca appear to be present. Most lines are narrow, and some of the broad ones are possible blends. Whenever the width turned out to be consistent with zero at the 90 per cent level, $\sigma = 2$ eV was assumed. This does not automatically imply that a line is unresolved, due to its low number of counts and significance. We will address this point again in the next Section.

Interestingly, all the continuum components were left

² A merged, low-resolution spectrum was extracted from the undispersed images, but is not discussed any further in this work.

free to vary and returned very sensible values (Table 1), leading to an excellent fit with $C/\nu = 442/434$. The photon index of the intrinsic AGN power-law emission is $\Gamma \simeq 2.10$, and the gas column density is $N_{\text{H}} \simeq 1.4 \times 10^{24} \text{ cm}^{-2}$; the absorption-corrected 2–10 keV flux is of the order of $\sim 10^{-11} \text{ erg s}^{-1} \text{ cm}^{-2}$, in keeping with the historical behaviour of NGC 1365. The strength of the reflection component is ordinary as well, $R \simeq 1$, and only ~ 1 per cent of the primary AGN continuum is scattered back into our line of sight. As for the collisionally ionized plasma, its characteristic temperature converges to $kT \simeq 1 \text{ keV}$, contributing to most of the Fe L-shell forest and to some extent also to the Ly α lines from the main α -elements (see above). With this respect, the spectral parameters reported in Table 2 only refer to the photoionized component. Below we discuss in greater detail the properties of the various lines and their implications on the physical conditions of the emitting gas.

4 DISCUSSION

When seen at high resolution, the soft X-ray spectra of obscured active galaxies display a wealth of narrow emission lines with little or no continuum, arising from low-temperature ($T < 10^5 \text{ K}$, or a few eV) gas photoionized and photoexcited by the primary nuclear radiation (e.g. Sako et al. 2000; Kinkhabwala et al. 2002; Schurch et al. 2004). *Chandra* images have also revealed the substantial spatial extension of the soft X-ray emission, and its striking correlation with the size and morphology of the Narrow Line Region (NLR) as mapped by *HST* in the [O III] $\lambda 5007$ line (Ogle et al. 2000; Bianchi, Guainazzi & Chiaberge 2006). This suggests that the same gas shines in both [O III] and soft X-rays. In general, the latter can also be a signature of mechanical and shock heating in star-forming regions, yet the contribution from collisionally ionized plasma is usually minor (Brinkman et al. 2002). Although detailed spectral diagnostics are available for the handful of brightest sources only (e.g. Kallman et al. 2014), this trend seems to apply to the entire population of local type 1.5–2 Seyfert galaxies, with just a few exceptions (Guainazzi & Bianchi 2007). NGC 1365 stands out among the peculiar objects by virtue of the foremost influence of thermal plasma on its RGS spectrum. According to Guainazzi et al. (2009), evidence for photoionized matter solely relies on excess emission in the forbidden (f) and intercombination (i) components of O VII He α , in N VI He α (f), and in the tentative O VII and O VIII radiative recombination continua (RRC).

The new *Chandra*/HETG observations take advantage of a much better angular resolution, and allowed us to ignore the bulk of the circumnuclear starburst. The resultant spectra cannot be explained through a multi-temperature gas in collisional equilibrium, whose importance is conversely highly diminished. The emergence of the diluted emission from a photoionized region closer to the hard X-ray source tends to reconcile the nature of NGC 1365 with the average properties of the local obscured AGN. In order to move towards a self-consistent description of the whole sequence of lines in Table 2, we removed all the Gaussian profiles from model E (except for Fe I K α) and generated several sets of photoionization grids with XSTAR (Kallman & Bautista 2001). We adopted an optical to X-ray spec-

tral energy distribution similar to the one used in Guainazzi et al. (2009), based on an $\alpha_{\text{ox}} = 1.5$ energy index,³ and on a 1–1000 Rydberg (13.6 eV to 13.6 keV) luminosity of $\sim 10^{44} \text{ erg s}^{-1}$. For each turbulence velocity broadening of 500, 1000, 1500 and 2000 km s^{-1} (1σ), the grids cover five orders of magnitude in both column density and ionization parameter,⁴ with $5 \times 10^{19} < N_{\text{H}}/\text{cm}^{-2} < 5 \times 10^{24}$ and $0 < \log(\xi/\text{erg cm s}^{-1}) < 5$, respectively. We also tested different gas densities, typical of BLR and NLR clouds, with indistinguishable results.

The inclusion of any photoionized component was accepted as significant after a statistical improvement of $\Delta C = -13.3$, corresponding to the 99 per cent confidence level for four parameters of interest, i.e. N_{H} , ξ , normalization and outflow velocity. As expected, no exhaustive solution was found in this effort, which should be merely taken as a rudimentary proof of the existence of a fairly large range of ionization states. This notwithstanding, a passable fit ($C/\nu = 605/479$) was achieved with three emission phases with $\log(\xi/\text{erg cm s}^{-1}) > 4.1$, $\sim 3.1 \pm 0.3$, and < 0.6 . The other gas properties are not well constrained (especially the column densities), so we refrain from discussing their face values. Anyway, there is evidence for motions along the line of sight: two XSTAR components have a modest outflow velocity of $v_{\text{out}} = 850_{-330}^{+620} \text{ km s}^{-1}$, while the third one prefers an inflow at $\sim 3500 \text{ km s}^{-1}$ to a systemic velocity ($\Delta C = 7$). This is driven by the broad complex centred at $E \sim 555 \text{ eV}$ (Table 2) and its identification with O VII He α , which is not fully reliable (see below). In this model, once the threefold AGN continuum is excluded, the contribution from collisionally ionized plasma to the 0.5–4 keV flux is about 30 per cent. Overall, the main shortcoming is that the intensity of many of the former Gaussian lines is slightly underpredicted, possibly due to higher metallicity. A $3\times$ solar Fe abundance in the nuclear region of NGC 1365 is indeed suggested by the X-ray reflection features (Risaliti et al. 2009b; Brenneman et al. 2013).

4.1 Line properties

For the sake of a qualitative assessment, we subsequently considered both the MEG and HEG spectra at 1024 and 2048 channels, preserving the constant resolution in wavelength space afforded by the gratings. This choice is not suitable for global statistical purposes, since no photons are collected in several bins, especially at very low or high energies. Moreover, because of the low number of counts, the aspect and position of some lines is contingent on the binning criterion adopted. While some degree of speculation is admitted in this heuristic approach, we always checked the raw data in wavelength units to avoid exotic interpretations, sticking to the most conservative explanation. None the less, in many cases this helped us extracting more detailed information on the properties of the emission lines, for instance in terms of widths, velocity shifts and relative weight of the

³ The spectral index $\alpha_{\text{ox}} = -0.384 \log(L_{2 \text{ keV}}/L_{2500 \text{ \AA}})$ is the usual indicator of the optical to X-ray luminosity ratio in AGN.

⁴ The ionization parameter is defined as $\xi = L_{\text{ion}}/nr^2$, where n is the gas electron density and r is its distance from the source with 1–1000 Ry luminosity L_{ion} .

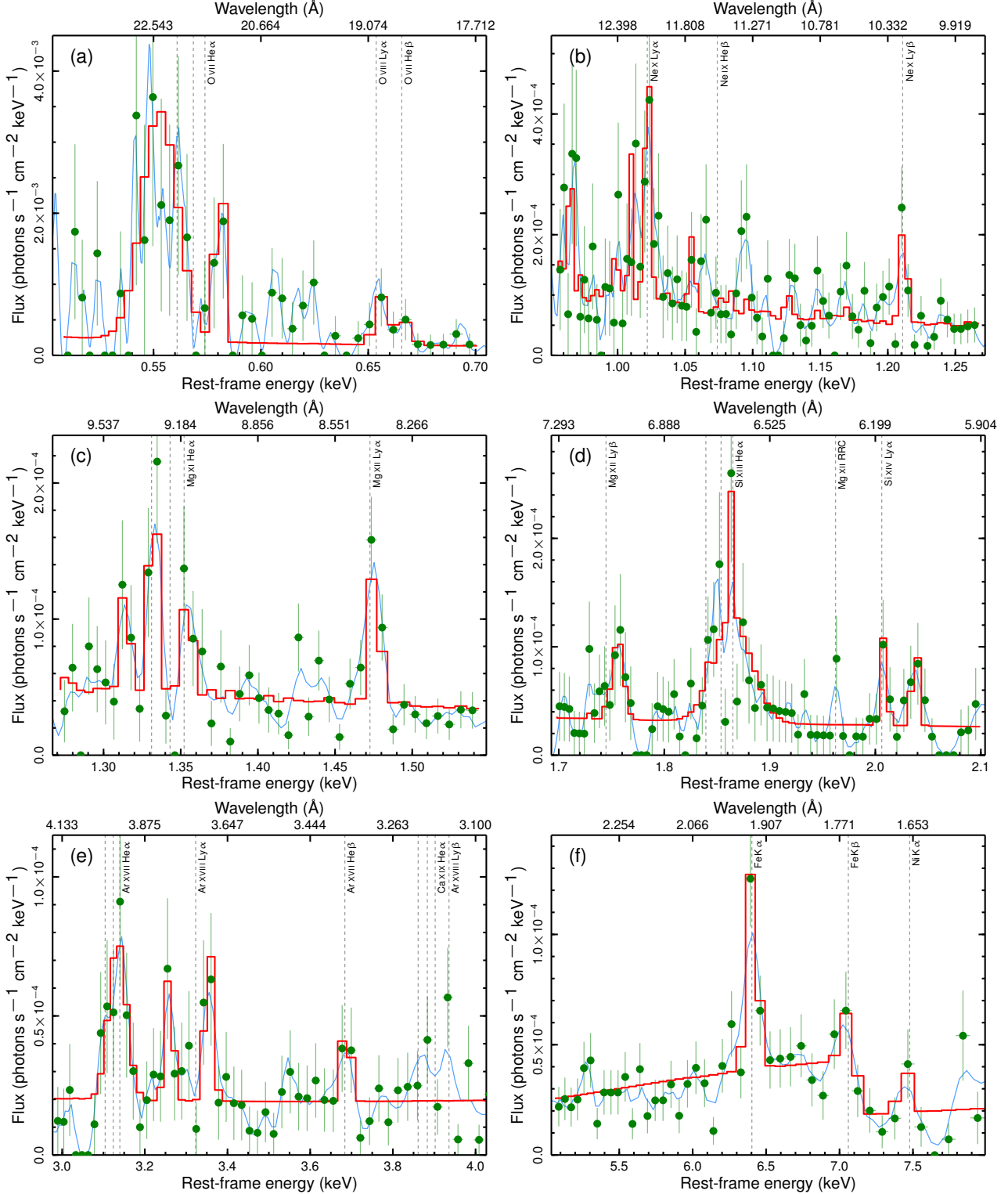


Figure 4. Enlarged view of the MEG (a–c) and HEG (d–f) spectra in the main emission bands. The thermal and AGN continuum components were assumed from model E, while the lines were refitted (red curve). The data were rebinned to 1024 channels, corresponding to ~ 2 times the native FWHM resolution. For the sake of a visual inspection, a 5-channel wide triangular smoothing has been applied to the ungrouped spectra (turquoise curve). The vertical lines mark the expected energy of the stronger transitions. (a) Due to the poor signal to noise, the sampling in the oxygen band is further degraded to a factor of 8, with a smoothing window of 13 channels. (b) Both Ne x Ly α and Ly β are detected with a possible velocity broadening (FWHM ~ 1300 km s $^{-1}$). The thermal component is not able to fully account for all the putative Fe lines. (c) Despite the triplet-like appearance of the emission complex at ~ 1.31 – 1.36 keV, the lower-energy line is not associated with Mg xi He α and is most likely due to Fe xxi $4d \rightarrow 2p$. (d) The broad resonance line of Si xiii can be resolved into a blueshifted ($v_{\text{out}} \sim 1600$ km s $^{-1}$) triplet. (e) The double peak across Ar xviii Ly α would imply inflows/outflows at several thousands km s $^{-1}$, but the red horn is not confirmed in the MEG data. (f) Besides the resolved Fe K α feature, both Fe K β and Ni K α are clearly present although statistically not significant due to the low effective area over this range. (See the text for more details).

different components in He-like triplets. To this aim, we also created smoothed spectral profiles by applying a triangular moving average to the unbinned (2048 channels) data. For each band of interest, the results of this procedure are shown in Fig. 4, where the baseline continuum is drawn from model E and the key features have been fitted afresh. In the following we examine every atomic species separately, and then try to infer a more general picture.

4.1.1 Oxygen

Unfortunately, at the energies of the O VII–VIII emission the MEG spectrum is extremely noisy, and perhaps also affected by some background. In this case, we had to rebin down to 256 channels and perform a comparably heavy smoothing (Fig. 4a). Even so, it is clear that the broad feature at ~ 555 eV in model E (which could be blindly associated with O V $K\alpha$ from its centroid) presents several substructures, and that the line at $E \sim 618$ eV in Table 2 (in formal agreement with O V $K\beta$) is actually a blend (possibly including N VII $Ly\gamma$). We attempted at fitting the former complex with a self-consistent O VII He α triplet, fixing the energy of the three components and allowing for a common shift. As anticipated above, this selects a redshift with velocity of ~ 5500 km s $^{-1}$, which would be loosely supported by the identification of the line at $E \simeq 581$ eV (falling just below our detection threshold) with N VII $Ly\beta$ ($E \simeq 593$ eV at rest). Bearing in mind some claims in this sense (like for Mrk 110; Boller, Balestra & Kollatschny 2007), such a fast inflow is not regarded as genuine in this context, and the ~ 555 -eV blend remains ambiguous. We note that one of the spikes in the smoothed spectrum has the right energy for the forbidden component of the oxygen He-like triplet, but other species might be involved (for example, N VI RRC is found at 552 eV). The statistics are seriously deficient, but the feature at $E \simeq 581$ eV can be tentatively ascribed to outflowing O VII. Also the O VIII $Ly\alpha$ line suggests a $v_{\text{out}} \sim 500 \pm 200$ km s $^{-1}$, and the higher order $Ly\beta$, $Ly\gamma$ and RRC transitions of this ion are consistent with this value,⁵ even if suffering from contamination by the Fe L-shell array.

4.1.2 Neon

There is very little evidence for Ne IX emission, once the almost coincident $3d \rightarrow 2p$ lines from Fe XIX are attributed to collisionally ionized gas. Ne X $Ly\alpha$ and $Ly\beta$, instead, are both obvious and definitely interesting. They appear to be resolved ($\sigma = 1.9_{-0.5}^{+0.7}$ eV for $\Delta C = 1$) and minimally blueshifted ($v_{\text{out}} < 400$ km s $^{-1}$; Table 3). The intensity ratio $Ly\beta/Ly\alpha$ is quite large, $\sim 0.6 \pm 0.3$. This is a hint of photoexcitation, which boosts the higher order lines through radiative decay (e.g. Kinkhabwala et al. 2002). Also Fe L-shell resonances would be enhanced (Sako et al. 2000), and indeed the thermal component fails to reproduce their emission at ~ 1.06 – 1.18 keV (Fig. 4b). Notably, the strongest $3d \rightarrow 2p$ Fe lines, including Fe XX (0.956 keV) and Fe XXI (1.009 keV), accept some blueshift at $v_{\text{out}} \sim 900$ km s $^{-1}$. This is probably too high (e.g. Veilleux, Cecil & Bland-Hawthorn 2005)

⁵ In the O VIII energy range, the MEG absolute wavelength accuracy is equivalent to ~ 200 km s $^{-1}$.

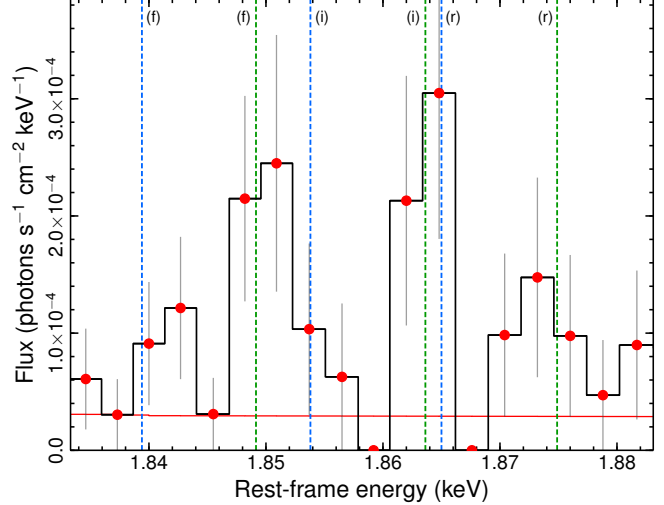


Figure 5. Si XIII He α triplet in the HEG spectrum at 2048 channels ($\Delta\lambda \simeq 10$ mÅ, consistent with the FWHM resolution). The blue and green dashed lines indicate the energy of the forbidden, intercombination, and resonance transitions for $v_{\text{out}} = 0$ and 1600 km s $^{-1}$, respectively. Both velocity components seem to be present within the energy/wavelength calibration accuracy, the former possibly associated with the starburst and the latter to the AGN. The continuum is drawn in red.

for any starburst superwind in NGC 1365, favouring an origin from matter photoionized and photoexcited by the AGN rather than shock-heated much farther out.

4.1.3 Magnesium

Three lines are seen in the Mg XI He α band (Fig. 4c), but the low-energy one is actually due to Fe XXI $4d \rightarrow 2p$, again more prominent than in a pure thermal scenario. The remaining pair are presumably the forbidden and recombination components of the triplet. Together with the Mg XII $Ly\alpha$ line, they share $\sigma = 1.6 \pm 0.6$ eV ($\Delta C = 1$) and $v_{\text{out}} \sim 700 \pm 100$ km s $^{-1}$ (Table 3). The only other feature from these ions is the possible Mg XII RRC, while the puzzling excess around the energy of the $Ly\beta$ is formally incompatible with the shift of the parent series, and is eventually unknown (Fig. 4d).

4.1.4 Silicon

A broad line is detected in model E at the energy of Si XIII He α , centred around the resonance transition. Its width in the HEG spectrum at 1024 channels is $\sigma \sim 18$ eV, and a narrow core is noticeable (Fig. 4d). While the FWHM of ~ 7000 km s $^{-1}$ would dictate a BLR origin, we tried to disentangle the triplet components. The best solution is found for unresolved profiles at $v_{\text{out}} \sim 1600 \pm 100$ km s $^{-1}$, with the forbidden and resonance lines shifted to ~ 1.850 and 1.875 keV (Fig. 5). This outflow velocity is not confirmed by Si XIV $Ly\alpha$, which lies at the expected rest-frame energy. Moreover, after the joint ~ 10 -eV shift, the intercombination line becomes the stronger one at ~ 1.865 keV, which is inconsistent with the weights of Mg XI and practically unphysical. On the other hand, its intensity is naturally explained by a contribution from resonant emission at rest, supported by the faint forbidden companion and associated with either the AGN

Table 3. Summary of the best constrained lines. No errors are given for tied (or frozen) parameters. Uncertainties are purely statistical at the 68 per cent confidence level ($\Delta C = 1$).

Line	E_{lab} (keV)	σ (eV)	FWHM (km s ⁻¹)	v_{out} (km s ⁻¹)
Ne x Ly α	1.022	$1.9^{+0.7}_{-0.5}$	1280^{+480}_{-510}	< 400
Ne x Ly β	1.211	2.1	1280	< 400
Mg xi He α (f)	1.331	1.6 ± 0.6	840^{+300}_{-320}	710 ± 110
Mg xi He α (r)	1.352	1.6	840	710
Mg xii Ly α	1.473	1.8	840	710
Si xiii He α (f)	1.839	< 1.6	< 600	1590^{+80}_{-60}
Si xiii He α (r)	1.865	< 1.6	< 600	1590
Si xiv Ly α	2.006	< 1.7	< 600	< 300

or the starburst. Two velocity components are tentatively distinguished then. Only the properties of the blueshifted triplet are listed in Table 3. Finally, there is an unidentified secondary peak at $E \sim 2.039$ keV. The closer transition is Al xiii Ly β ($E \simeq 2.048$ keV), but any Ly α counterpart would be much weaker. If due to H-like silicon, the sizable shift calls for $v_{\text{out}} \sim 4700$ km s⁻¹.

4.1.5 Argon

While S xv–xvi is recognized but very faint, some basic constraints can be put on Ar xvii–xviii. The broad ($\sigma \sim 17$ eV) He α line is found again at the resonance energy. The same considerations made above for the Si triplet could apply, but here any fine structure cannot be appreciated since the separation of the three components is commensurate with the FWHM. The same holds for He β . Another double-peaked feature is visible across the Ar xviii Ly α transition (Fig. 4e). The red horn is dubious, since the HEG and MEG data are in conflict (the MEG resolution, however, is lower by a factor of 2). The blue one would correspond to $v_{\text{out}} \sim 2700$ km s⁻¹. In any case, we can rule out a contribution of the Ar xviii Ly β line (3.936 keV at rest) to the blend near ~ 3.90 keV, which is the alleged combination of forbidden and resonant Ca xix He α with modest blueshift.

4.1.6 Iron

Above 4 keV, only the fluorescence K α line from neutral iron at $E = 6.404^{+0.012}_{-0.015}$ is statistically significant, although the K β is clear as well, and there is a trace of Ni K α (Fig. 4f). All of these are signatures of reflection of the AGN radiation in cold, optically thick matter, arguably located at the torus scale in the original unification scheme. We can assess the distance of this gas from the width of the Fe K α line, which is nicely resolved thanks to its ~ 35 –40 counts ($\sigma = 27^{+17}_{-12}$ eV; Fig. 6). We assume that the broadening is due to the virial motion in the emitting region, and that the velocity dispersion is related to the FWHM through a factor $f = \sqrt{3}/2$, which corrects for the (unknown) geometry and distribution of the gas (see also Netzer & Marziani 2010). The predicted FWHM is $\sim 760(M_8/r_{\text{pc}})$ km s⁻¹, where M_8 is the mass of the central black hole in units of $10^8 M_{\odot}$ and r_{pc} is the radial distance in pc. This expression agrees within a factor of ~ 2 with the case of pure Keplerian motion with

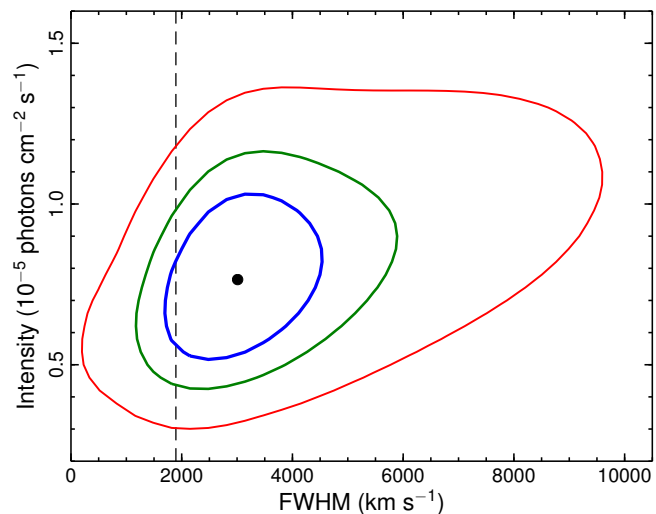


Figure 6. Confidence contours at the nominal 68, 90 and 99 per cent level for the Fe K α intensity versus velocity width, obtained from the unbinned HEG spectrum with all the AGN continuum parameters free to vary. The vertical dashed line indicates the FWHM of the broad H β component in the optical, suggesting a common origin from BLR clouds.

reasonable orbital inclination ($i > 20^\circ$). Far larger uncertainties are associated with the black hole mass. No direct measurement (e.g. from reverberation mapping) is available for NGC 1365, so that the full range of $\log(M_{\text{BH}}/M_{\odot}) \sim 6$ –8 is covered in the literature. The higher values are based on the correlation of M_{BH} with the bulge luminosity, and are likely biased by the starburst contribution to the latter. The most sensible guess is then of a few $\times 10^6 M_{\odot}$ (Risaliti et al. 2009b; Davis et al. 2014). With a conservative $M_8 = 0.1$, and the observed K α FWHM of $\sim 3000^{+1900}_{-1350}$ km s⁻¹, we obtain that $r \sim 0.002$ – 0.02 pc, which is within the BLR. Indeed, the width of the K α line is consistent (at 90 per cent errors) with that of the broad nuclear component of the H β in the optical, whose FWHM is 1895 km s⁻¹ (Schulz et al. 1999). From the K α /H β width ratio we can deduce that the relative size of the respective emission regions is roughly the same. This is not surprising in a source like NGC 1365, where BLR clouds are responsible for variable X-ray obscuration up to the Fe-K band and beyond. Regardless of the precise black hole mass, in terms of the gravitational radius the distance of the Fe K α reflector perfectly agrees with the universal location of a few $\times 10^4 r_g$ determined by Shu, Yaqoob & Wang (2011).

4.2 Covering factor

As established from the FWHM of Fe K α (3000 km s⁻¹) and, provisionally, from those of Ne x (~ 1300 km s⁻¹) and Mg xii Ly α (~ 800 km s⁻¹), the gas probed by these Chandra/HETG spectra is likely located across the boundary between the classical BLR and NLR (see also Crenshaw & Kraemer 2007). It is therefore tempting to try to evaluate its covering fraction (f_{cov}) and to explore its connection with the clumps responsible for the X-ray occultations of the source. To do so, we applied an XSTAR grid to the 1.3–1.5 keV band, characterized by the intense lines from Mg xi–xii.

For given column density and amount of ionizing radiation, the measured Mg luminosity of $L_{\text{Mg}} \sim 6 \times 10^{38} \text{ erg s}^{-1}$ depends on the fraction of solid angle occupied by the gas. The predicted luminosity for a full covering of $4\pi \text{ sr}$ (i.e., $f_{\text{cov}} = 1$) is degenerate with the column density, but becomes slowly responsive to its exact value at $N_{\text{H}} > 2 \times 10^{23} \text{ cm}^{-2}$, which is typical for BLR clouds in NGC 1365 (Risaliti et al. 2009b). In that range, the entailed f_{cov} lies between $\sim 2\text{--}7 \times 10^{-3}$. This is not far from the NLR covering factor delivered by photoionization models, which, however, is thought to be substantially underestimated (Netzer & Laor 1993). Indeed, it should be quite similar to the BLR one ($\sim 0.2\text{--}0.4$; e.g. Korista, Ferland & Baldwin 1997), even if showing a stronger decreasing trend with luminosity (Stern & Laor 2012). A column of $\sim 10^{21} \text{ cm}^{-2}$, still plausible for the NLR, would be needed to match the expectations.

There are several caveats about this simple calculation, though. For instance, the nearly equivalent intensity of the He α (f) and Ly α lines requires a fine tuning of $\log(\xi/\text{erg cm s}^{-1}) \sim 3.5$ in a single-zone model. If a wider range of ionization states is involved, f_{cov} can be considerably higher. Allowing for two components with $N_{\text{H}} = 5 \times 10^{22} \text{ cm}^{-2}$ and $\log(\xi/\text{erg cm s}^{-1}) = 2.5$ and 4.5 , respectively, returns a better fit and a covering fraction of ~ 0.15 . Many other configurations are viable, and also a mild attenuation of L_{Mg} by an external absorption layer, maybe at host-galaxy scales, cannot be ruled out. Alternatively, given the narrower profile of the Mg lines compared to Fe K α , we can speculate that the innermost clouds significantly reduce the ionizing flux seen by the emitting gas at larger distance, thus producing an apparently low f_{cov} for the NLR. For $\log(\xi/\text{erg cm s}^{-1}) \sim 3.5$ and $n \sim 10^5 \text{ cm}^{-3}$, Mg emission would occur at $r \sim 0.2 \text{ pc}$, at least an order of magnitude higher than what inferred for Fe K α (remarkably proportional to the square of the FWHM ratio). This is the most intriguing explanation, since it is consistent with the under-luminosity in the soft X-ray oxygen lines noted by Guainazzi et al. (2009), despite the fact that the AGN in NGC 1365 is not intrinsically weak. Unfortunately, the current data quality does not warrant any conclusive answer.

4.3 Temperature and density

The presence of possible RRC from species like O VIII or Mg XII implies that the emitting gas has a low temperature and that the ionization state is regulated by radiation rather than by collisional equilibrium. Radiative recombination, in fact, is the emission of a photon following the capture of a free electron, mainly to the ground state of an ion. The shape of the consequent feature is a powerful diagnostic of the gas temperature. In a cold plasma, only the tail of high-energy electrons overcome the recombination threshold, and the RRC have a narrow, line-like profile, whose width is $\Delta E \sim kT$ (Hatchett, Buff & McCray 1976; Liedahl & Paerels 1996). Both detections in proximity of O VIII and Mg XII RRC rely on $\sim 6\text{--}7$ line counts only in the MEG and HEG data, respectively. Hence we cannot disentangle the putative O VIII RRC from the nearby Fe XVIII L-shell transition, in particular if the former is moderately blueshifted. No blend with other strong lines is instead foreseen at the energy of Mg XII RRC, yet we remind that this feature is not statistically significant, so we were only able to put an

upper limit of 3 eV (or $3.5 \times 10^4 \text{ K}$; $\Delta C = 1$) with a **redge** model.

More information can be potentially derived by the He-like triplets, consisting of the resonance ($1s2p \ ^1P_1 \rightarrow 1s^2 \ ^1S_0$), intercombination ($1s2p \ ^3P_{2,1} \rightarrow 1s^2 \ ^1S_0$), and forbidden ($1s2s \ ^3S_1 \rightarrow 1s^2 \ ^1S_0$) transitions. These provide an effective measure of the physical conditions of the gas (Porquet & Dubau 2000, and references therein), since the intensity ratios $\mathcal{R} = f/i$ and $\mathcal{G} = (f+i)/r$ are very sensitive to the electron density and temperature, respectively. Given that O VII is too noisy, Ne IX is formally undetected, and S XVII, Ar XVII and Ca XIX are too faint and/or unresolved, the only accessible species are Mg XI and Si XIII. Even if the triplet decompositions proposed above (which impose outflow velocities of $\sim 700 \text{ km s}^{-1}$ for Mg and $\sim 1600 \text{ km s}^{-1}$ for Si) are valid, only upper limits can be placed. The density can be anything below the critical value ($n \sim 10^{13}\text{--}10^{14} \text{ cm}^{-3}$) beyond which the forbidden components are collisionally suppressed, while temperature is constrained to be $T < 3 \times 10^6 \text{ K}$. This is barely meaningful in the light of the appearance of narrow RRC features, but it is enough to exclude collisional ionization in a hot ($kT \sim 1 \text{ keV}$) plasma as the dominant mechanism in these emission-line HETG spectra of NGC 1365.

5 SUMMARY AND CONCLUSIONS

In this paper we have presented the X-ray spectral analysis of the first *Chandra*/HETG observations of the prototypical changing-look Seyfert galaxy NGC 1365, which lingered in a Compton-thick state for the entire span of four days. The soft X-ray spectrum was thus dominated by a wealth of recombination lines belonging to He- and H-like ions of the most common light elements from oxygen to calcium, plus iron L-shell transitions. Thanks to the unrivaled spatial resolution offered by *Chandra*, we were able to zoom in on the close surroundings of the AGN, and unveil a photoionized gas component that was largely diluted in previous observations. Indeed, the spectra obtained with *XMM-Newton*/RGS, whose large aperture also encompasses all the diffuse emission from the inner 5 kpc, were heavily contaminated by collisionally ionized plasma, shock-heated by the fierce circumnuclear star-formation activity. The residual thermal contribution to the overall emission-line intensity now amounts to ~ 30 per cent only.

The emergence of a photoionized spectrum with properties analogous to those reported in most of the nearby obscured Seyfert galaxies partly mitigates the apparent anomaly of NGC 1365. In spite of the modest statistical quality of the data, whereby only a handful of lines have > 10 counts, the picture in favour of cold ($kT \ll E$) gas exposed to the AGN radiation is corroborated by the tentative presence of narrow RRC features (O VIII and Mg XII), and by the qualitative inspection of the He-like triplets (mainly from Mg and Si). Photoexcitation might be important as well, as indicated by the strength of some higher order transitions (e.g. Ne X Ly β) and of the Fe L-shell forest around $\sim 1 \text{ keV}$. Possible outflow velocities in the range $\sim 0\text{--}1600 \text{ km s}^{-1}$ are revealed, and a few lines (Ne X, Mg XI–XII) show some evidence of broadening ($\sim 1000 \text{ km s}^{-1}$), signifying that the location of the gas is across the virtual BLR/NLR

boundary. The $K\alpha$ fluorescence feature from neutral iron at $E = 6.404^{+0.012}_{-0.015}$ keV is resolved to a width of $\sigma = 27^{+17}_{-12}$ eV, corresponding to a FWHM of $\sim 3000^{+1900}_{-1350}$ km s $^{-1}$. This is somewhat larger but fully consistent with the optical H β line, supporting a comparable size of the emitting regions. With a preferential distance of few $\times 10^4 r_g$ from the black hole, it is then very likely that Fe $K\alpha$ arises from the same Compton-thick clouds that induce the recurrent column density jumps and the extreme variability seen in this source.

Besides the main findings, there are also some unusual hints, such as of broad (BLR-like) profiles in resonance lines, of double peaks, and of radial velocities of several thousands km s $^{-1}$, even in inflow. If confirmed, these would be absolutely exceptional traits, but caution is mandatory given the poor statistics. As opposed to standard type-2 Seyferts like NGC 1068, the erratic behaviour of NGC 1365 below 10 keV makes it hard to amass strictly consistent information from different epochs, so naively it could seem unfeasible to overcome this limitation with just a longer exposure. However, even in a Compton-thin case, the column density is normally of the order of $N_H \sim 10^{23}$ cm $^{-2}$, and the direct AGN continuum is almost completely absorbed in the soft X-rays. The ample record of past observations suggests that a nearly unobserved state such as the one sampled in January 2013 is a very rare occurrence for NGC 1365. The photoelectric cutoff is thus expected to fall beyond the main complexes from O, Ne, Mg, and maybe also Si, leaving their aspect virtually constant with time and allowing the build-up of a nuclear emission-line template. On the other hand, the appearance of the transmitted AGN continuum at higher energies would enable the study of the high-ionization absorption features originating from the accretion-disc/BLR wind, from Fe XXV–XXVI down to Ca XIX–XX and even Ar XVII–XVIII, depending on the exact value of N_H . For these reasons, any prospective observation of NGC 1365 at high spatial and spectral resolution would provide further invaluable insights into the properties of the sub-pc scale environment in active galaxies.

ACKNOWLEDGMENTS

We thank the anonymous referee for their useful comments. EN is supported by STFC under grant ST/J001384/1. JNR acknowledges the financial support provided through the *Chandra* award GO2-13123A for this programme. The scientific results reported in this article are based on observations made by the *Chandra* X-ray Observatory. This research has made use of software provided by the *Chandra* X-ray Center (CXC) in the application package CIAO. The figures were generated using *matplotlib* (Hunter 2007), a PYTHON library for publication of quality graphics.

REFERENCES

Alonso-Herrero A., et al., 2012, MNRAS, 425, 311
 Antonucci R., 1993, ARA&A, 31, 473
 Antonucci R. R. J., Miller J. S., 1985, ApJ, 297, 621
 Bianchi S., Guainazzi M., Chiaberge M., 2006, A&A, 448, 499
 Bianchi S., Maiolino R., Risaliti G., 2012, AdAst, 2012, 782030
 Boller T., Balestra I., Kollatschny W., 2007, A&A, 465, 87
 Braiton V., Reeves J. N., Gofford J., Nardini E., Porquet D., Risaliti G., 2014, ApJ, 795, 87

Brenneman L. W., Risaliti G., Elvis M., Nardini E., 2013, MNRAS, 429, 2662
 Brinkman A. C., Kaastra J. S., van der Meer R. L. J., Kinkhabwala A., Behar E., Kahn S. M., Paerels F. B. S., Sako M., 2002, A&A, 396, 761
 Canizares C. R., et al., 2005, PASP, 117, 1144
 Cash W., 1979, ApJ, 228, 939
 Connolly S. D., McHardy I. M., Dwelly T., 2014, MNRAS, 440, 3503
 Crenshaw D. M., Kraemer S. B., 2007, ApJ, 659, 250
 Davis B. L., et al., 2014, ApJ, 789, 124
 Guainazzi M., Bianchi S., 2007, MNRAS, 374, 1290
 Guainazzi M., Risaliti G., Nucita A., Wang J., Bianchi S., Soria R., Zezas A., 2009, A&A, 505, 589
 Hatchett S., Buff J., McCray R., 1976, ApJ, 206, 847
 Hunter J. D., 2007, CSE, 9, 90
 Kaastra J. S., et al., 2004, A&A, 428, 57
 Kalberla P. M. W., Burton W. B., Hartmann D., Arnal E. M., Bajaja E., Morras R., Pöppel W. G. L., 2005, A&A, 440, 775
 Kallman T., Bautista M., 2001, ApJS, 133, 221
 Kallman T., Evans D. A., Marshall H., Canizares C., Longinotti A., Nowak M., Schulz N., 2014, ApJ, 780, 121
 Kinkhabwala A., et al., 2002, ApJ, 575, 732
 Korista K., Ferland G., Baldwin J., 1997, ApJ, 487, 555
 Krolik J. H., Begelman M. C., 1988, ApJ, 329, 702
 Landi E., Del Zanna G., Young P. R., Dere K. P., Mason H. E., 2012, ApJ, 744, 99
 Liedahl D. A., Paerels F., 1996, ApJ, 468, L33
 Madore B. F., et al., 1998, Natur, 395, 47
 Magdziarz P., Zdziarski A. A., 1995, MNRAS, 273, 837
 Maiolino R., Rieke G. H., 1995, ApJ, 454, 95
 Maiolino R., et al., 2010, A&A, 517, A47
 Matt G., Guainazzi M., Maiolino R., 2003, MNRAS, 342, 422
 Netzer H., 2015, arXiv, arXiv:1505.00811
 Netzer H., Laor A., 1993, ApJ, 404, L51
 Netzer H., Marziani P., 2010, ApJ, 724, 318
 Ogle P. M., Marshall H. L., Lee J. C., Canizares C. R., 2000, ApJ, 545, L81
 Porquet D., Dubau J., 2000, A&AS, 143, 495
 Risaliti G., Bianchi S., Matt G., Baldi A., Elvis M., Fabbiano G., Zezas A., 2005, ApJ, 630, L129
 Risaliti G., Elvis M., Fabbiano G., Baldi A., Zezas A., Salvati M., 2007, ApJ, 659, L111
 Risaliti G., et al., 2009a, MNRAS, 393, L1
 Risaliti G., et al., 2009b, ApJ, 696, 160
 Rivers E., et al., 2015, ApJ, 804, 107
 Sako M., Kahn S. M., Paerels F., Liedahl D. A., 2000, ApJ, 543, L115
 Schulz H., Komossa S., Schmitz C., Mücke A., 1999, A&A, 346, 764
 Schurch N. J., Warwick R. S., Griffiths R. E., Kahn S. M., 2004, MNRAS, 350, 1
 Shu X. W., Yaqoob T., Wang J. X., 2011, ApJ, 738, 147
 Smith R. K., Brickhouse N. S., Liedahl D. A., Raymond J. C., 2001, ApJ, 556, L91
 Stern J., Laor A., 2012, MNRAS, 426, 2703
 Veilleux S., Cecil G., Bland-Hawthorn J., 2005, ARA&A, 43, 769
 Wang J., Fabbiano G., Elvis M., Risaliti G., Mazzarella J. M., Howell J. H., Lord S., 2009, ApJ, 694, 718
 Wilms J., Allen A., McCray R., 2000, ApJ, 542, 914